Article

Force Analysis and Strength Determination of the Cemented Paste Backfill Roof in Underhand Drift Cut-and-Fill Stopping

Yafei Hu [1,2], Bin Han [1,2,*], Bo Zhang [1,2] and Keqing Li [1,2]

[1] School of Civil and Resource Engineering, University of Science and Technology Beijing, Beijing 100083, China
[2] Key Laboratory of Ministry of Education of China for Efficient Mining and Safety of Metal Mines, University of Science and Technology Beijing, Beijing 100083, China
* Correspondence: bin.han@ustb.edu.cn

Abstract: The stability of the cemented paste backfill roof (CPB roof) is critical to safe production in mines using the underhand drift cut-and-fill stopping. To investigate the scientific and reasonable design method of key parameters (size and strength) of the CPB roof and the stress state of the CPB roof during the mining process, field measurements were carried out with Jinchuan Group's third mining area as the engineering background. Based on the measurement results, a mechanics model was constructed based on the thick plate theory. The field measurement results show that the overlying load on the CPB roof tends to increase first and then decrease with the gradual mining of the stope, and the maximum overlying load values of the two CPB roofs measured are 0.240 MPa and 0.244 MPa, respectively. With the gradual mining of the stope, the deformation of the CPB roof shows a trend of increasing first and then stabilizing. Based on the thick plate theory, the stress model of the CPB roof is constructed, and the error between the calculation results of the model and the field measurement results does not exceed 5%. Applying the research results to the three mines of Jinchuan Group, the span of the stope can be expanded from 5 m to 6 m under the existing strength standard of the filling body, which can increase its mining capacity by 20%. This study is the first to measure the overlying load and the tensile stress value on the CPB roof, which is an important guideline for related theoretical research.

Keywords: filling mining; backfill strength; mechanical model; thick plate theory; field measurements

1. Introduction

With the rapid development of the world economy, the consumption of mineral resources is increasing, which has put forward higher requirements for the development of the mining industry [1,2]. However, with the increasing depletion of mineral resources and the growing importance of environmental protection, there is an urgent need to solve the problem of how to develop and utilize mineral resources safely and efficiently [3–5]. Due to the advantages of high safety, high recovery rate and low damage to the surface environment, the filling mining method is preferred by more and more mines [6–8].

This research focuses on the underhand drift cut-and-fill stopping [9,10]. This method is mainly used for metal deposits where both the ore and the surrounding rock are unstable or where the ore is of high value and high grade [11,12]. Although the underhand drift cut-and-fill stopping has the outstanding advantages of flexible stope layout and excellent applicability to complex fractured rocks, it also has the problems of relatively high mining costs and low mining efficiency [13,14]. Since miners need to work under the filling body, if the filling body is too strong, it can increase the mining cost, and if the filling body is too weak, it can be a safety hazard [15,16]. It is generally accepted that the larger the size of the stope the higher the strength of the filling body required, but there is no scientific basis for matching the relationship between stope size and filling body parameters [17–20]. Therefore, it is important to study the relationship between the size of different mining

fields and the strength of the filling body, and to propose a reasonable design method for the size of the mining field and the strength of the filling body for safe and efficient recovery of the mine.

Most existing studies on the strength design of filling bodies focus on theoretical calculations and numerical simulations [21–24]. The thin plate theory model and beam theory model are the most commonly used force models for the top plate of the filling body [25]. Chang et al. derived the relationship between the thickness of the CPB roof, CPB tensile strength and overlying load q based on the combined beam theory, and obtained the minimum thickness to satisfy the stability requirement of the CPB roof [26]. Sun et al. constructed a computational model of the tensile forces on the CPB roof based on the elastic thin plate theory, and obtained that the damage mode of the CPB roof is dominated by tensile damage, which mainly occurs in the middle of the lower surface of the CPB roof. In addition, the study also shows that the tensile strength of the CPB roof is linearly and positively correlated with the overlying load q [27]. Zhu et al. show that when the thickness-to-span ratio of CPB roofs is larger than 1/4, large errors occur when using the elastic thin plate theory as well as the elastic beam theory for the strength design of the filling body, and other methods need to be used for the relevant design at this time [28]. The results of existing studies show that the main factors affecting the strength of the filling body are structural parameters (size of the stope, thickness and span of the CPB roof) and physical and mechanical parameters of the ore body and overlying load. In engineering practice, the structural parameters and the physical and mechanical parameters of the ore body are easy to obtain, but the overlying load is difficult to determine [29].

By summarizing the existing studies, it is found that the overlying load of the CPB roof cannot be accurately calculated yet, which would negatively affect the determination of the strength of CPB roof. Based on this, this study is the first to accurately determine the overlying load of the CPB roof by in situ measurement, which can provide data support for reasonable determination of stope size and strength of the filling body. Based on the field measurements, a calculation model of the force on the filling body based on the thick plate theory is constructed, which avoids the calculation errors existing in the existing elastic beam and plate theory and provides theoretical support for the scientific design of key mining parameters. This research's results can guide the safe and efficient production of underhand drift cut-and-fill stopping.

2. Field Measurements

2.1. Introduction to the Case Study

Located in Gansu Province, China, Jinchuan Group is a large nickel-based mining company that ranked first in China in terms of nickel production in 2021. After more than sixty years of practice and exploration, Jinchuan Group has developed the largest mechanized underhand drift cut-and-fill stopping with the largest continuous recovery area in the world. The third mine of Jinchuan Group was taken as an example, which adopts the mechanized panel area downward layered cement filling mining method. The panel areas are divided along the strike of the ore body, each panel area is 100 m~200 m long and the width is the horizontal thickness of the ore body, and each panel area is connected by a segmented liaison road and a layered liaison road. The height of the drift-type stope is 4.5 m, the span is 5 m and the length generally is not more than 70 m. Cemented paste backfill (CPB) is used to fill the mining-out area, and the compressive strength and tensile strength of CPB are 5 MPa and 0.59 MPa, respectively. As can be seen from Figure 1, workers are exposed to the CPB roof for mining operations, thus the mechanical properties of the CPB roof are extremely important for safe mining. To investigate the stress–strain distribution pattern in the CPB roof during mining, field measurements were conducted in the 40# stope of the third sublevel of the 1110 m sub-section II panel area third mine and the 48# stope of the third sublevel of the third panel area.
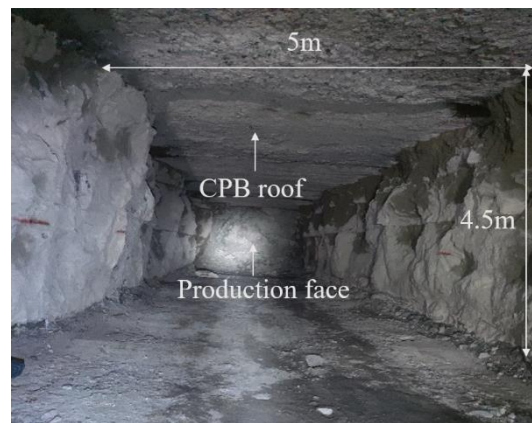
Figure 1. Drift-type stope.

2.2. Measurement Equipment and Solutions

Existing studies show that the stresses on the CPB roof are mainly related to the size of the stope, the physical and mechanical properties of the CPB and the overlying load on the CPB roof [30]. The dimensions of the stope and the physical and mechanical properties of the CPB are easier to obtain, while the stresses on the CPB roof and the overlying load on the CPB roof are obtained by field measurements [31–34].

2.2.1. Measurement Equipment

The measurement devices are mainly vibrational chord strain gauges and string pressure sensors, and the relevant parameters are shown in Table 1. The strain gauge is used to measure the strain and stress within the CPB roof during the mining process, and its model number is YHZ-0130. The strain gauge is buried in CPB with a range of $\pm$ 1500 micrometer strain ($\mu\varepsilon$), a resolution of 1 $\mu\varepsilon$ and an accuracy of $\pm$ 0.5% full-scale (F.S). The strain change within the CPB roof is measured by this strain gauge, and the strain can be converted to stress by Equation (1).

$$\sigma = E \cdot \varepsilon \tag{1}$$

where σ is the stress in the CPB roof, E is the elastic modulus of the CPB roof and ε is the strain in the CPB roof.

Table 1. Main parameters of the measurement equipment.

Type	Appearance	Model Number	Measurement Range	Resolution	Precision/%FS
Strain gauge		YHZ-0130	$\pm$1500 $\mu\varepsilon$	1 $\mu\varepsilon$	$\pm$0.5
Pressure sensor		YHZ-0701	1 MPa	0.1 KPa	$\pm$0.5

The pressure sensor is used to measure the load inside the CPB roof during the mining process and its model number is YHZ-0701. The sensor is buried in concrete sustaining a maximum pressure of up to 1 MPa with a resolution of 0.1 KPa and an accuracy of $\pm$ 0.5% F.S.

2.2.2. Measurement Solutions

The installation sites for the measurement equipment are the 46# stope of the third layer of the III panel area of the 1110 m section and 33# stope of the third layer of the II panel area of the 1110 m section of the 3rd mine. After the 46# and 33# stopes are mined, a mining-out area is formed. The measurement equipment was then buried in the CPB by fixing it in the mining-out area through a steel frame and then filling the mining-out

area with CPB. The sensors buried in the CPB roof above start collecting measurement data when mining takes place in the 48# and 40# stopes, and the next layers in the 46# and 33# stopes. The length of 48# stope is 35.0 m and the 40# stope is 40 m. The buried depths of the strain gauges in the CPB roof are 0.5 m, 1 m and 1.5 m, respectively, and the buried depths of pressure transducers in the CPB roof are 1 m, 2 m and 3 m, respectively. The measurement scheme and the installation process on site are shown in Figure 2 and Table 2. To avoid damage to the data transmission line during mining, the cable was packed into a steel tube for protection. Data were collected using a data collector when the stope started re-mining and date collected was stopped when the re-mining was completed.
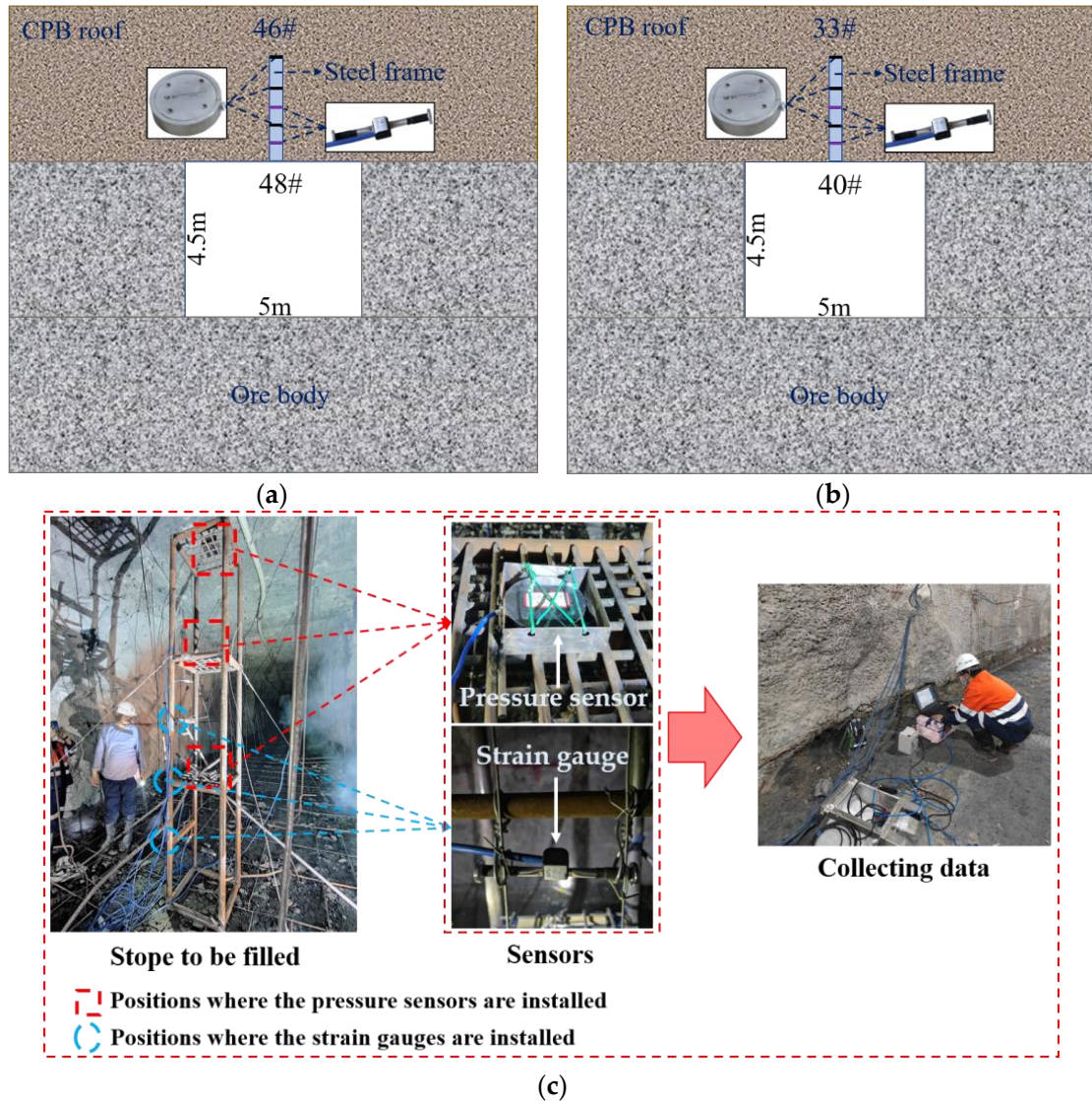
Figure 2. Measurement solutions: (**a**) 48# stope, (**b**) 40# stope, (**c**) measurement process.

Table 2. Measurement solutions.

Stope	Size/m (Length × Width × Height)	Measurement Solutions			
		Type	Buried Depth/m	Type	Buried Depth/m
48#	35 × 5.0 × 4.5	Load	1.0/2.0/3.0	Stress/Strain	0.5/1.0/2.0
40#	40 × 5.0 × 4.5				

3. Results and Analysis

3.1. Distribution Pattern of the Load on the CPB Roof during the Mining Process

The measured overlying load on the CPB roof during the mining process is shown in Figure 3. From Figure 3, it can be seen that the overlying load values measured by the three sensors buried at different locations of the CPB roof tend to increase and then decrease with the advancement of the production face. The overlying load value measured by the sensors is the largest when the production face advances below the buried position of the sensors. As the mining face continues to advance, the overlying load on the CPB roof decreases rapidly due to the formation of a pressure arch in the CPB roof, and eventually stabilizes under the unloading effect. The maximum overlying load values measured by the sensors buried 1 m, 2 m and 3 m from the lower surface of the CPB roof in 48 # stope are 0.240, 0.237 and 0.228 MPa, respectively, while the maximum overlying load values measured by the sensors buried 1 m, 2 m and 3 m from the lower surface of the CPB roof in the 40# stope are 0.244, 0.239 and 0.228 MPa, respectively. After mining, the overlying load on the CPB roof of the 48# stope is stabilized at about 0.193 MPa, and the overlying load on the CPB roof of the 40# stope is stabilized at about 0.194 MPa.
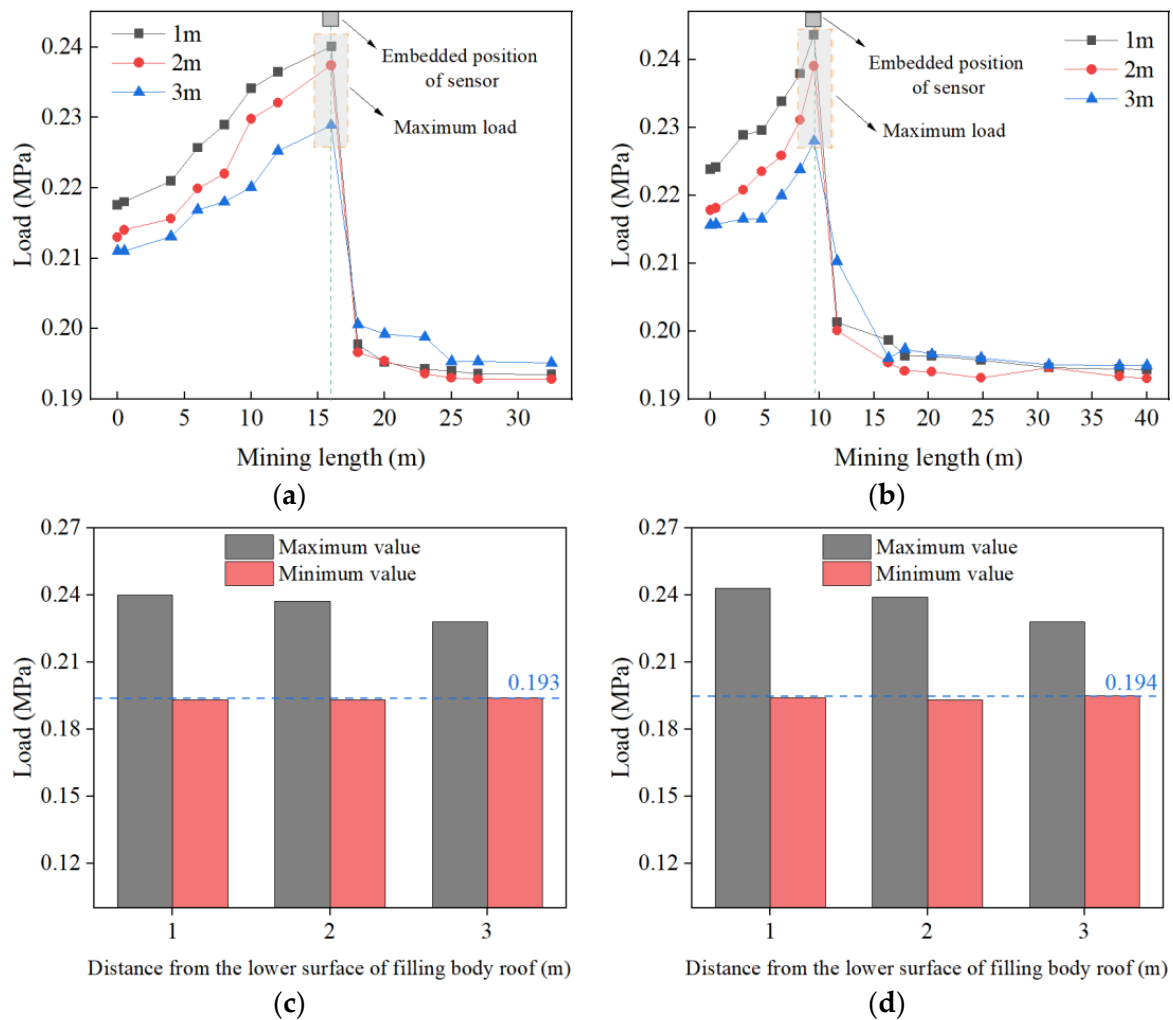
Figure 3. Results of load measurement: (**a**) 48# stope, (**b**) 40# stope, (**c**) maximum and minimum load values of 48# stope, (**d**) maximum and minimum load values of 40# stope.

3.2. Stress–Strain Evolution Pattern of CPB Roof during Mining

The stress–strain measurements of the CPB roof during mining in the stope are shown in Figure 4. From Figure 4, it can be seen that the stress–strain within the CPB roof tends to

increase first and then gradually stabilize as the mining length increases. In the process of advancing the production face to the buried position of the sensor, the stress–strain in the CPB roof tends to increase gradually, and the closer the production face is to the buried position of the sensor, the more significant the trend of increasing stress–strain. The stress–strain in the CPB reaches a maximum when the mining faces advance below the buried position of the sensor. Meanwhile, the closer to the lower surface of the CPB roof, the higher the stress–strain. As the production face continues to advance, the increase in stress–strain in the CPB decreases and gradually stabilizes. The maximum stress and strain of the CPB roof in the 48# stope are 0.344 MPa and 125 $\mu\varepsilon$, respectively, and the maximum stress and strain of the CPB roof in the 40# stope are 0.357 MPa and 130 $\mu\varepsilon$, respectively. Comparing the stress–strain measurements of the 48# stope and 40# stope, it can be seen that when the length of the stope is increased from 35 m to 40 m, the maximum stress and strain increase by 3.8% and 4.0%, respectively. This indicates that the length of the stope affects the stresses and strains in the CPB roof, but the affectivity is relatively low, which is generally in agreement with the measurements of the loads applied to the CPB.
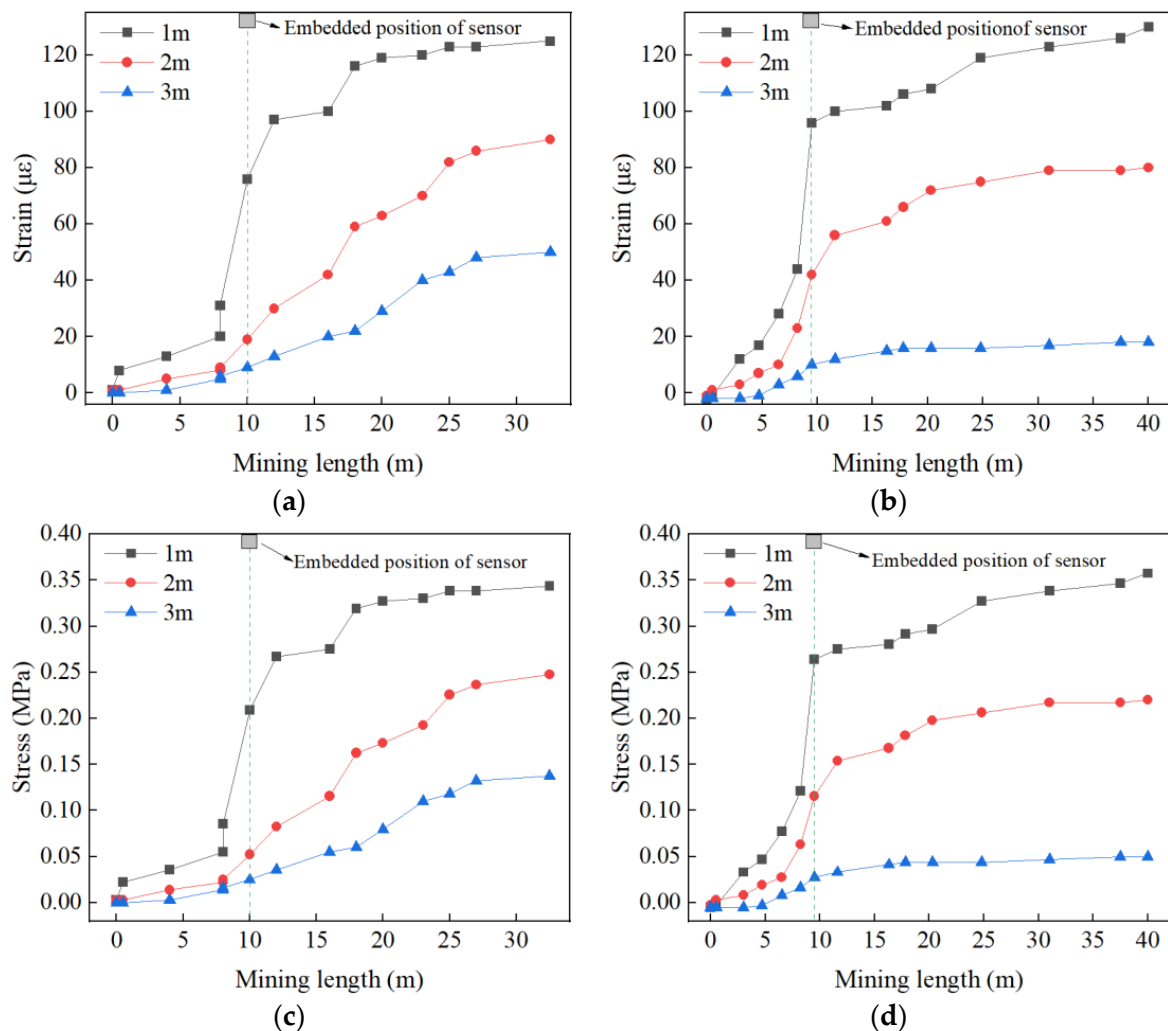
Figure 4. Results of stress–strain measurements: (**a**,**c**) are the strains and stresses in 48# stope, (**b**,**d**) are the strains and stresses in 40# stope, respectively.

3.3. Theoretical Analysis

3.3.1. Calculation of Overlying Load of CPB Roof

The overlying load on the CPB roof is the vertical load acting on the CPB roof after mining the stope. There are many theoretical formulas for determining the overlying load

of CPB roofs, but the different factors (the size of the stope, the physical and mechanical properties of the CPB and the overlying load on the CPB roof) considered in each formula lead to large differences in the calculated results [35–39]. This study investigates the theory of optimal CPB roof overburden calculation based on the field measurements and the engineering characteristics of the downward mining method [40–44].

The more commonly used calculation theories are Platts theory of ground pressure, the Biebermann pressure theory, the Classical Janssen pressure theory and the Terzaghi bearing capacity theory, whose calculation models are shown in Equations (2)–(5) [45–47]. The Biebermann pressure theory, Classical Janssen pressure theory and Terzaghi bearing capacity theory take into account the size of the stope, the physical and mechanical properties of the filling body and the effect of the height of the overburdened filling body on the load, and their calculation methods are more reasonable. Although the Platts theory of ground pressure takes into account the size of the approach stope and the physical and mechanical properties of the filling body, it does not consider the key factor of the height of the overburdened filling body, so its calculation results are somewhat one-sided.

(1) Platts theory of ground pressure:

$$q = \frac{\gamma \left[a + h \tan\left(45° - \frac{\varphi}{2}\right) \right]}{f} \tag{2}$$

In Equation (2), q is the load on the CPB roof, h is the height of the stope, a is the span of the stope, γ is the capacity of the filling body, φ is the friction angle in the filling body and f is the solidity factor.

(2) Biebermann pressure theory:

$$\left. \begin{aligned} q &= \gamma H \left[1 - \frac{H}{a_1} K_1 - \frac{2c}{a_1 \gamma} (1 - 2K_2) \right] \\ a_1 &= a + 2h \tan\left(45° - \frac{\varphi}{2}\right) \\ K_1 &= \tan\varphi \tan^2\left(45° - \frac{\varphi}{2}\right) \\ K_2 &= \tan\varphi \tan\left(45° - \frac{\varphi}{2}\right) \end{aligned} \right\} \tag{3}$$

In Equation (3), H is the buried depth, c is the cohesion of the filling body and a is the span of the stope.

(3) Classical Janssen pressure theory:

$$q = \frac{\gamma S}{k \tan\varphi p} \left[1 - \exp\left(-\frac{kpH \tan\varphi}{S} \right) \right] \tag{4}$$

In Equation (4), S is the horizontal section area of the stope ($s = a \times b$), b is the length of the stope, p is the perimeter of the horizontal section of the stope and k is the lateral pressure coefficient.

(4) Terzaghi bearing capacity theory:

$$q = \frac{\gamma a_1 - c}{k \tan\varphi} \left[1 - \exp\left(-\frac{kH \tan\varphi}{a_1} \right) \right] \tag{5}$$

3.3.2. Evaluation of the Applicability of the Model

The overburden height H of the downward drift cut-and-fill stopping mining method is the product of the height h of the filled individual stopes and the number of filling layers m. Taking the stopes of the third mining area of Jinchuan Group as an example, the overburden filling body has a capacitance γ of 20 KN/m^3, an internal friction angle φ of 31° and a cohesion force of 1180 KPa, and the load on the CPB roof is obtained by substituting Equations (2)–(5) as shown in Figure 5a. From Figure 5a, it can be seen that the load values obtained based on Platts theory of ground pressure are constant, which is because the effect of filling body height is not considered in this theoretical model. The load value obtained based on the Terzaghi bearing capacity theory increases with the increase in the number of

layers of the filled body and then stabilizes, but the load value is negative, which is due to the fact that the theoretical model is affected by the cohesive force. The load value obtained based on the Biebermann pressure theory increases and then decreases with the increase in the number of layers of the filling body, which is not consistent with the actual situation. The load value obtained based on the Classical Janssen pressure theory increases with the increase in the number of layers of the filling body and then stabilizes, which is consistent with the conclusions obtained from the previous studies [48–51]. Therefore, the load values calculated based on Classical Janssen pressure theory are more suitable for the actual law.
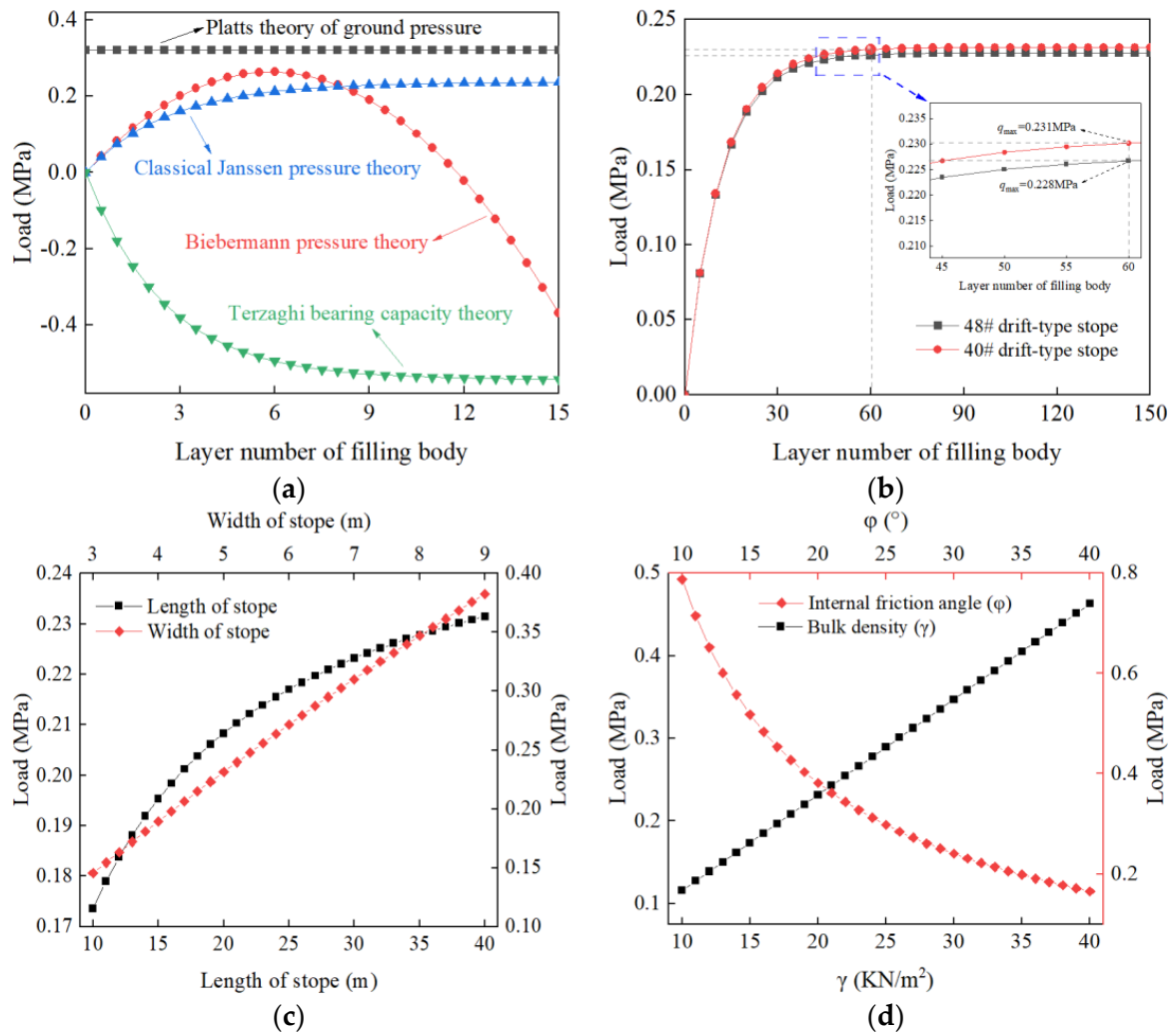
Figure 5. Results of load calculation: (**a**) comparison of each theory, (**b**) calculation results of experimental stopes, (**c**) effect of stope size on load, (**d**) effect of physical and mechanical parameters of the filling body on load.

The relationship between the number of layers of different filling bodies and the load on the filling body is obtained after substituting the relevant parameters of 48# and 40# stopes into Classical Janssen pressure theory (see Figure 5b). From Figure 5b, it can be seen that the load on the CPB roof reaches the limitation when the number of layers of the filling body is 60. When the number of layers of the filling body exceeds 60, the load no longer changes. The calculated extreme values of the loads on the CPB roofs of the 48# and 40# stopes are 0.228 MPa and 0.231 MPa, respectively, which are close to the measured values in the field. This indicates that the load on the filling body calculated by the Classical Janssen pressure theory is more reasonable.

The effects of different factors on the loads applied to the CPB roof are shown in Figure 5c,d. As the span of the stope increases, the load on the CPB roof shows a linear increase. When the span of the stopes is expanded from 3 m to 9 m, the load on the CPB roof is increased by 164%. As the length of the stope increases, the load on the CPB roof tends to increase rapidly and then stabilize. When the length of the stope exceeds 150 m, the load on the CPB roof reaches the extreme value. As the capacity of the filling body increases, the load on it tends to increase linearly. When the capacity is increased from 10 KN/m^2 to 40 KN/m^2, the load value is increased by 299%. With the increase in the friction angle in the filling body, the load on the CPB roof tends to decrease gradually. The above results are basically in agreement with the previous studies.

3.3.3. Analysis of Stresses on CPB Roof

The stress on the CPB roof is a key indicator for determining the strength of the filling body. This stress is affected by complex factors such as the overlying load of the CPB roof, the physical and mechanical parameters of the filling body and the dimensions of the stope, which makes it difficult to express accurately by a simple expression [52,53]. Currently, the simple beam theory and elastic thin plate theory are commonly used in engineering to calculate the stresses on CPB roofs. However, because the ratio of stope height to width for the underhand drift cut-and-fill stopping mining method is higher than 1/5, the results obtained by the above theoretical calculation deviate from the actual results. Based on this, the thick plate theory is introduced in this study to analyze the stresses on the CPB roof [54]. The CPB roof is simplified as a rectangular thick plate with four sides simply supported, and its mechanical model is shown in Figure 6.
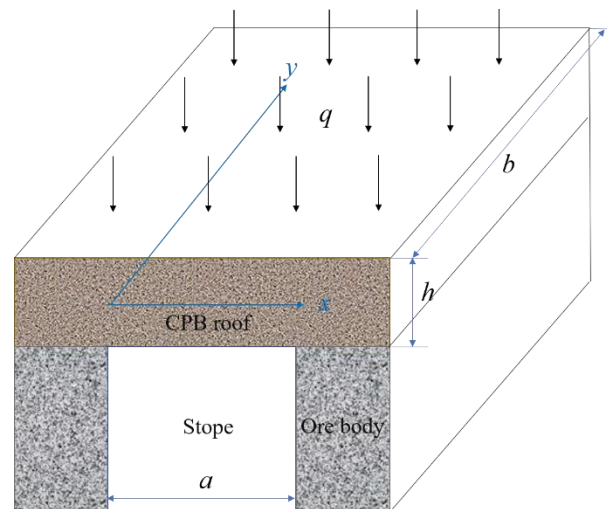
Figure 6. Mechanical model of CPB roof.

The four sides of the thick plate are simply supported boundaries, so the deflection, bending moment and rotation angle on the boundaries are all zero, which can be expressed as follow (1) at $x = 0$ and $x = a$:

$w = 0, M_x = 0, \psi_y = 0$

(2) at $y = 0$ and $y = b$:

$w = 0, M_y = 0, \psi_x = 0$

where b represents the length of the thick plate, a is the width of the thick plate, w is the deflection of the thick plate, M_x and M_y are the bending moments of the thick plate around the x-axis and y-axis, respectively, and ψ_x and ψ_y are the rotation angles of the thick plate around the x-axis and y-axis, respectively.

According to Vlasov's theory, the equilibrium differential equations for a simply supported rectangular thick plate are

$$\frac{D}{5}\left[(1-u)\nabla^2\psi_x + (1+u)\frac{\partial\Phi}{\partial x} + \frac{1}{2}\frac{\partial}{\partial x}\left(\nabla^2 w\right)\right] + \frac{Gh}{3}\left(\frac{\partial w}{\partial x} - \psi_x\right) = 0 \tag{6}$$

$$\frac{D}{5}\left[(1-u)\nabla^2\psi_y + (1+u)\frac{\partial\Phi}{\partial y} + \frac{1}{2}\frac{\partial}{\partial y}\left(\nabla^2 w\right)\right] + \frac{Gh}{3}\left(\frac{\partial w}{\partial y} - \psi_y\right) = 0 \tag{7}$$

where h is the thickness of the thick plate; μ is the Poisson's ratio of the thick plate; E is the modulus of elasticity of the thick plate and $\Phi = \frac{\partial\psi_x}{\partial x} + \frac{\partial\psi_y}{\partial y}$. D is the bending stiffness of the thick plate and G is the shear deformation modulus of the thick plate, which can be expressed as

$$D = \frac{Eh^3}{12(1-\mu^2)} \tag{8}$$

$$G = \frac{E}{2(1+\mu)} \tag{9}$$

Then, the internal forces and moments of the CTB roof are expressed as follows:

$$M_x = -\frac{D}{5}\left[4\left(\frac{\partial\psi_x}{\partial x} + \mu\frac{\partial\psi_y}{\partial y}\right) + \left(\frac{\partial^2 w}{\partial x^2} + \mu\frac{\partial^2 w}{\partial y^2}\right)\right] \tag{10}$$

$$M_y = -\frac{D}{5}\left[4\left(\frac{\partial\psi_y}{\partial y} + \mu\frac{\partial\psi_x}{\partial x}\right) + \left(\frac{\partial^2 w}{\partial y^2} + \mu\frac{\partial^2 w}{\partial x^2}\right)\right] \tag{11}$$

$$M_{xy} = -\frac{D(1-\mu)}{5}\left[2\left(\frac{\partial\psi_x}{\partial y} + \frac{\partial\psi_y}{\partial x}\right) + \frac{\partial^2 w}{\partial x\partial y}\right] \tag{12}$$

$$Q_x = \frac{2}{3}Gh\left(\frac{\partial w}{\partial x} - \psi_x\right) \tag{13}$$

$$Q_y = \frac{2}{3}Gh\left(\frac{\partial w}{\partial x} - \psi_y\right) \tag{14}$$

where M_{xy} is the moment of the thick plate and Q_x and Q_y are the shear forces along the x and y directions, respectively.

Based on the boundary conditions, it may be useful to set the displacement functions for the deflection and the angle of rotation to be

$$w = \sum_{m=1}^{\infty}\sum_{n=1}^{\infty} A_{mn}\sin\frac{m\pi x}{a}\sin\frac{n\pi y}{b} \tag{15}$$

$$\psi_x = \sum_{m=1}^{\infty}\sum_{n=1}^{\infty} B_{mn}\cos\frac{m\pi x}{a}\sin\frac{n\pi y}{b} \tag{16}$$

$$\psi_y = \sum_{m=1}^{\infty}\sum_{n=1}^{\infty} C_{mn}\sin\frac{m\pi x}{a}\cos\frac{n\pi y}{b} \tag{17}$$

where A_{mn}, B_{mn} and C_{mn} are coefficients related to the deformation of the thick plate; m and n are positive integers.

The boundary conditions of the plate are all satisfied, and the load is expanded into the form of a double triangular series

$$q(x,y) = \sum_{m=1}^{\infty}\sum_{n=1}^{\infty} q_{mn}\sin\frac{m\pi x}{a}\sin\frac{n\pi y}{b} \tag{18}$$

where $q(x,y)$ is the load function of the thick plate and q_{mn} is the coefficient of the double delta series.

Using the orthogonality of trigonometric functions, the q_{mn} can then be expressed as

$$q_{mn} = \frac{4}{ab} \int_0^a \int_0^b q(x,y) \sin \frac{m\pi x}{a} \sin \frac{n\pi y}{b} dxdy \tag{19}$$

Assuming a uniform load is distributed above the CTB roof, then

$$q(x,y) = q_0 \tag{20}$$

where q_0 is the maximum load.

Substituting Equation (20) into Equation (19) yields

$$q_{mn} = \frac{16q_0}{\pi^2 mn} \tag{21}$$

Substituting Equations (15)–(17) and (19) into the system of differential Equations (10)–(14), the expressions A_{mn}, B_{mn} and C_{mn} are obtained:

$$A_{mn} = \left\{ 1 + \frac{6D\pi^2}{5Gh} \left[\left(\frac{m}{a}\right)^2 + \left(\frac{n}{b}\right)^2 \right] \right\} \frac{q_{mn}}{D\pi^4 \left[(m/a)^2 + (n/b)^2 \right]^2} \tag{22}$$

$$B_{mn} = \left\{ 1 - \frac{3D\pi^2}{10Gh} \left[\left(\frac{m}{a}\right)^2 + \left(\frac{n}{b}\right)^2 \right] \right\} \frac{mq_{mn}}{aD\pi^3 \left[(m/a)^2 + (n/b)^2 \right]^2} \tag{23}$$

$$C_{mn} = \left\{ 1 - \frac{3D\pi^2}{10Gh} \left[\left(\frac{m}{a}\right)^2 + \left(\frac{n}{b}\right)^2 \right] \right\} \frac{nq_{mn}}{bD\pi^3 \left[(m/a)^2 + (n/b)^2 \right]^2} \tag{24}$$

With guaranteed accuracy, $m = n = 1$ is allowed, and then Equations (22)–(24) and (15)–(17) are combined to derive the expressions for the moments and deflections of the thick plate as the following:

$$w = \frac{16q_0}{D\pi^6} \left\{ \begin{array}{l} \left\{ 1 + \frac{6D\pi^2}{5Gh} \left[\left(\frac{1}{a}\right)^2 + \left(\frac{1}{b}\right)^2 \right] \right\} \frac{1}{\left[(1/a)^2 + (1/b)^2 \right]^2} \sin \frac{\pi x}{a} \sin \frac{\pi y}{b} \\ + \left\{ 1 + \frac{6D\pi^2}{5Gh} \left[\left(\frac{1}{a}\right)^2 + \left(\frac{3}{b}\right)^2 \right] \right\} \frac{1}{3 \left[(1/a)^2 + (3/b)^2 \right]^2} \sin \frac{\pi x}{a} \sin \frac{3\pi y}{b} \\ + \left\{ 1 + \frac{6D\pi^2}{5Gh} \left[\left(\frac{3}{a}\right)^2 + \left(\frac{1}{b}\right)^2 \right] \right\} \frac{1}{3 \left[(3/a)^2 + (1/b)^2 \right]^2} \sin \frac{3\pi x}{a} \sin \frac{\pi y}{b} \\ + \left\{ 1 + \frac{6D\pi^2}{5Gh} \left[\left(\frac{3}{a}\right)^2 + \left(\frac{3}{b}\right)^2 \right] \right\} \frac{1}{9 \left[(3/a)^2 + (3/b)^2 \right]^2} \sin \frac{3\pi x}{a} \sin \frac{3\pi y}{b} \end{array} \right\} \tag{25}$$

$$\psi_x = \frac{16q_0}{D\pi^5} \left\{ \begin{array}{l} \left\{ 1 - \frac{3D\pi^2}{10Gh} \left[\left(\frac{1}{a}\right)^2 + \left(\frac{1}{b}\right)^2 \right] \right\} \frac{1}{a \left[(1/a)^2 + (1/b)^2 \right]^2} \cos \frac{\pi x}{a} \sin \frac{\pi y}{b} \\ + \left\{ 1 - \frac{3D\pi^2}{10Gh} \left[\left(\frac{1}{a}\right)^2 + \left(\frac{3}{b}\right)^2 \right] \right\} \frac{1}{3a \left[(1/a)^2 + (3/b)^2 \right]^2} \cos \frac{\pi x}{a} \sin \frac{3\pi y}{b} \\ + \left\{ 1 - \frac{3D\pi^2}{10Gh} \left[\left(\frac{3}{a}\right)^2 + \left(\frac{1}{b}\right)^2 \right] \right\} \frac{1}{a \left[(3/a)^2 + (1/b)^2 \right]^2} \cos \frac{3\pi x}{a} \sin \frac{\pi y}{b} \\ + \left\{ 1 - \frac{3D\pi^2}{10Gh} \left[\left(\frac{3}{a}\right)^2 + \left(\frac{3}{b}\right)^2 \right] \right\} \frac{1}{3a \left[(3/a)^2 + (3/b)^2 \right]^2} \cos \frac{3\pi x}{a} \sin \frac{3\pi y}{b} \end{array} \right\} \tag{26}$$

$$\psi_y = \frac{16q_0}{D\pi^5} \left\{ \begin{array}{l} \left\{1 - \frac{3D\pi^2}{10Gh}\left[\left(\frac{1}{a}\right)^2 + \left(\frac{1}{b}\right)^2\right]\right\} \frac{1}{b\left[(1/a)^2 + (1/b)^2\right]^2} \sin\frac{\pi x}{a}\cos\frac{\pi y}{b} \\[2ex] + \left\{1 - \frac{3D\pi^2}{10Gh}\left[\left(\frac{1}{a}\right)^2 + \left(\frac{3}{b}\right)^2\right]\right\} \frac{1}{b\left[(1/a)^2 + (3/b)^2\right]^2} \sin\frac{\pi x}{a}\cos\frac{3\pi y}{b} \\[2ex] + \left\{1 - \frac{3D\pi^2}{10Gh}\left[\left(\frac{3}{a}\right)^2 + \left(\frac{1}{b}\right)^2\right]\right\} \frac{1}{3b\left[(3/a)^2 + (1/b)^2\right]^2} \sin\frac{3\pi x}{a}\cos\frac{\pi y}{b} \\[2ex] + \left\{ \frac{1}{3b\left[(3/a)^2 + (3/b)^2\right]^2} \sin\frac{3\pi x}{a}\cos\frac{3\pi y}{b} \right. \end{array} \right\} \tag{27}$$

Substituting Equations (25)–(27) into Equations (6) and (7), respectively, it is clear that the bending moment has maximum values at $x = a/2$ and $y = b/2$, which can be expressed as

$$M_{x\max} = \frac{16q_0}{\pi^4} \left\{ \begin{array}{l} \frac{b^2 + \mu a^2}{a^2 b^2\left[(1/a)^2 + (1/b)^2\right]^2} - \frac{b^2 + 9\mu a^2}{3a^2 b^2\left[(1/a)^2 + (3/b)^2\right]^2} \\[2ex] - \frac{9b^2 + \mu a^2}{3a^2 b^2\left[(3/a)^2 + (1/b)^2\right]^2} + \frac{b^2 + \mu a^2}{a^2 b^2\left[(3/a)^2 + (3/b)^2\right]^2} \end{array} \right\} \tag{28}$$

$$M_{y\max} = \frac{16q_0}{\pi^4} \left\{ \begin{array}{l} \frac{a^2 + \mu b^2}{a^2 b^2\left[(1/a)^2 + (1/b)^2\right]^2} - \frac{9a^2 + \mu b^2}{3a^2 b^2\left[(1/a)^2 + (3/b)^2\right]^2} \\[2ex] - \frac{a^2 + 9\mu b^2}{3a^2 b^2\left[(3/a)^2 + (1/b)^2\right]^2} + \frac{a^2 + \mu b^2}{a^2 b^2\left[(3/a)^2 + (3/b)^2\right]^2} \end{array} \right\} \tag{29}$$

The maximum tensile stresses that occur at the lower surface of the CTB roof are calculated according to the following formulas (y direction):

$$\sigma_{\max}\big|_{z=\frac{h}{2}} = \frac{12M_{y\max}}{h^3}z \tag{30}$$

Then, the maximum tensile stresses in the CTB roof are

$$\sigma_{\max} = \frac{96q_0}{\pi^4 h^2} \left\{ \begin{array}{l} \frac{a^2 + \mu b^2}{a^2 b^2\left[(1/a)^2 + (1/b)^2\right]^2} - \frac{9a^2 + \mu b^2}{3a^2 b^2\left[(1/a)^2 + (3/b)^2\right]^2} \\[2ex] - \frac{a^2 + 9\mu b^2}{3a^2 b^2\left[(3/a)^2 + (1/b)^2\right]^2} + \frac{a^2 + \mu b^2}{a^2 b^2\left[(3/a)^2 + (3/b)^2\right]^2} \end{array} \right\} \tag{31}$$

During the bending process of the CPB roof, tensile damage occurs when the maximum tensile stress in the CPB roof exceeds the designed tensile strength of the CPB.

3.3.4. Evaluation of the Applicability of the Model

Taking the stope in the third mine of Jinchuan Group as an example, the Poisson's ratio μ of its CPB roof is 0.21, and the effects of different factors on the stresses on the CPB roof are obtained by substituting Equation (2), as shown in Figure 7. As the span of the stope increases, the stress on the CPB roof tends to increase gradually. When the span of the stope is expanded from 3 m to 6 m, the stress on the CPB roof is increased by 292%, which indicates that the span of the stope has a significant effect on the stress. With the increase in the length of the stope, the stresses on the CPB roof show a slow increasing trend. When the length of the stope is increased by 100%, the stress on the CPB roof only increases by 41%, which indicates that the effect of the length of the stope on the stress is low. As the height of the CPB roof increases, the stress on it tends to decrease gradually. With the increase in Poisson's ratio of the filling body and the overlying load of the filling body, the stress on the CPB roof tends to increase linearly. The stress distribution pattern of CPB roofs obtained based on the thick plate theory agrees with the engineering practice.
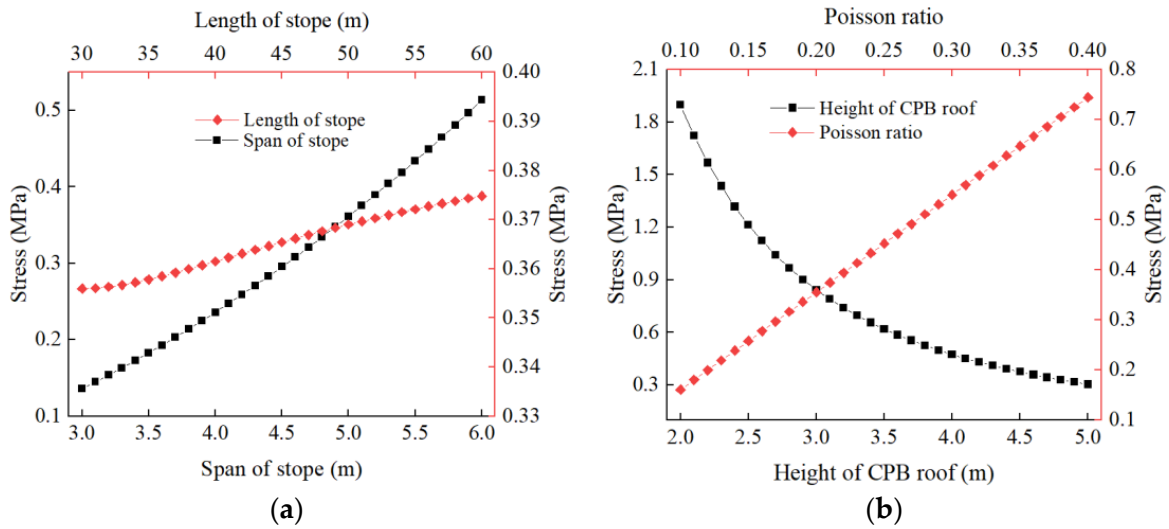
Figure 7. Effect of factors on stress: (**a**) size of the stope, (**b**) parameters of the filling body.

3.3.5. Examination of the Mechanical Model of the Filling Body

The CPB roof of the drift-type stope is mainly subject to tensile damage, and since the tensile strength of the filling body is low, it is reasonable to carry out the parameter design of a drift-type stope with tensile strength as the index. In this study, by comparing different mechanical models of the filling body and combining the field test results, the calculation model of the load on the filling body of the drift-type stope is determined, and the calculation model of the tensile stress on the filling body is also obtained based on the thick plate theory (see Equation (32)). Combining the two models, a mechanical model of the filling body subjected to a tension based on the parameters of the stope and the physical mechanical parameters of the filling body can be further obtained, as shown in Equation (33). The parameters in Equation (33) are simple and easy to obtain, which can guide the design of filling mining more easily.

$$
\begin{cases}
q_{\max} = \dfrac{\gamma S}{k \tan \varphi p}\left[1 - \exp\left(-\dfrac{kpH \tan \varphi}{S}\right)\right] \\[2mm]
\sigma_{\max} = \dfrac{96 q_{\max}}{\pi^4 h^2}\left\{
\begin{aligned}
&\dfrac{a^2+\mu b^2}{a^2 b^2\left[(1/a)^2+(1/b)^2\right]^2} - \dfrac{9a^2+\mu b^2}{3a^2 b^2\left[(1/a)^2+(3/b)^2\right]^2} \\
&-\dfrac{a^2+9\mu b^2}{3a^2 b^2\left[(3/a)^2+(1/b)^2\right]^2} + \dfrac{a^2+\mu b^2}{a^2 b^2\left[(3/a)^2+(3/b)^2\right]^2}
\end{aligned}
\right\}
\end{cases}
\tag{32}
$$

$$
\sigma_t \geq \sigma_{\max} = \dfrac{96\gamma\left[1-\exp\left(-\dfrac{kpH \tan \varphi}{S}\right)\right]}{k\pi^4 ph^2 \tan \varphi} \times
\begin{cases}
\dfrac{a^2+\mu b^2}{ab\left[(1/a)^2+(1/b)^2\right]^2} - \dfrac{9a^2+\mu b^2}{3ab\left[(1/a)^2+(3/b)^2\right]^2} \\[2mm]
-\dfrac{a^2+9\mu b^2}{3ab\left[(3/a)^2+(1/b)^2\right]^2} + \dfrac{a^2+\mu b^2}{ab\left[(3/a)^2+(3/b)^2\right]^2}
\end{cases}
\tag{33}
$$

The calculated values of the loads and tensile stresses on the filling body are obtained by substituting the relevant parameters of the 48# stope and 40# stope into the calculation model, and the calculation results and the field measurement results are shown in Figure 8. From Figure 8a, it can be seen that the errors of the calculated values of the overlying loads on the CPB roofs of the 48# stope and 40# stope are 5.0% and 5.2%, respectively. From Figure 8b, it can be seen that the errors of the calculated values of the maximum tensile stresses applied are 4.1% and 2.5%, respectively. All errors are less than 6%, which indicates the high reliability of the mechanical model of the filling body.
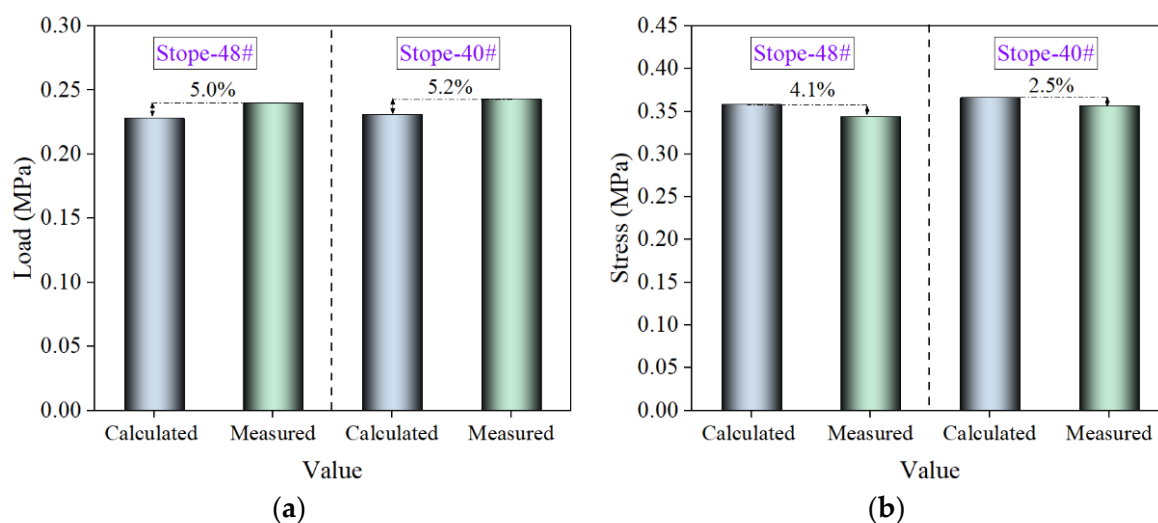
Figure 8. Comparison of calculation and measurement values: (**a**) load, (**b**) stress.

4. Discussion

4.1. Engineering Application

The tensile strength of the filling body at Jinchuan Group's third mine is 0.59 MPa, while the results of field measurements and theoretical calculations show that the maximum tensile stress to which the filling body is subjected is less than 0.25 MPa, which means that the strength standard set by the mine is 2.36 times the actual required strength. The higher the strength of the filling body, the higher the consumption of cement and the higher the filling cost. Therefore, with the current mining process, the mine would add significant additional material costs when using the current strength standards. In addition, the production capacity of the mine is constrained by the section of the stope, and if the section of the stope can be expanded, the production capacity and productivity of the mine can be significantly improved. Based on the force model of the filling body, it is known that the larger the section size is, the higher the tensile strength of the filling body required. With the tensile strength of the filling body in the current mine being much higher than the actually required strength, it is feasible to expand the size of the section of the stope. Considering the adaptability of underground mechanical equipment in mining operations, instead of increasing the height of the stope, the span of the field is to be expanded. Substituting the relevant parameters into Equation (7), it can be seen that the span of the stope can be increased from 5 m to 6 m under the current strength standard of the filling body, at which time the tensile stress on the filling body is 0.57 MPa. This means that the tensile stress on the CPB roof is lower than the tensile strength of the CPB and the CPB roof can remain stable.

4.2. Stability Monitoring

The industrial test of large section mining was conducted in the 24# and 39# stopes of the second layer of the 1110 m section of panel area III in the third mining area to test the stability of the large-section stope. The monitoring points were arranged in the experimental stope, the convergence value of the stope was measured using a JSS30A digital convergence meter, and the results are shown in Figure 9. As can be seen from Figure 9, with the increase in mining length, the deformation of the mining-out area shows a trend of first increasing and then gradually stabilizing. After mining is completed, the maximum sinkage of the top plate is 9.44 mm and the maximum convergence of the two gangs is 8.14 mm, and the stope is kept stable with such little deformation. In addition, among the three deformation monitoring points set in the top plate, the deformation of the monitoring point located in the middle is the largest, which is in agreement with the deformation pattern of the thick plate model. The results of field experiments show that it

is feasible to increase the span of the third mining area from 5 m to 6 m, and the results also validate the reliability of the mechanical model of the filling body.
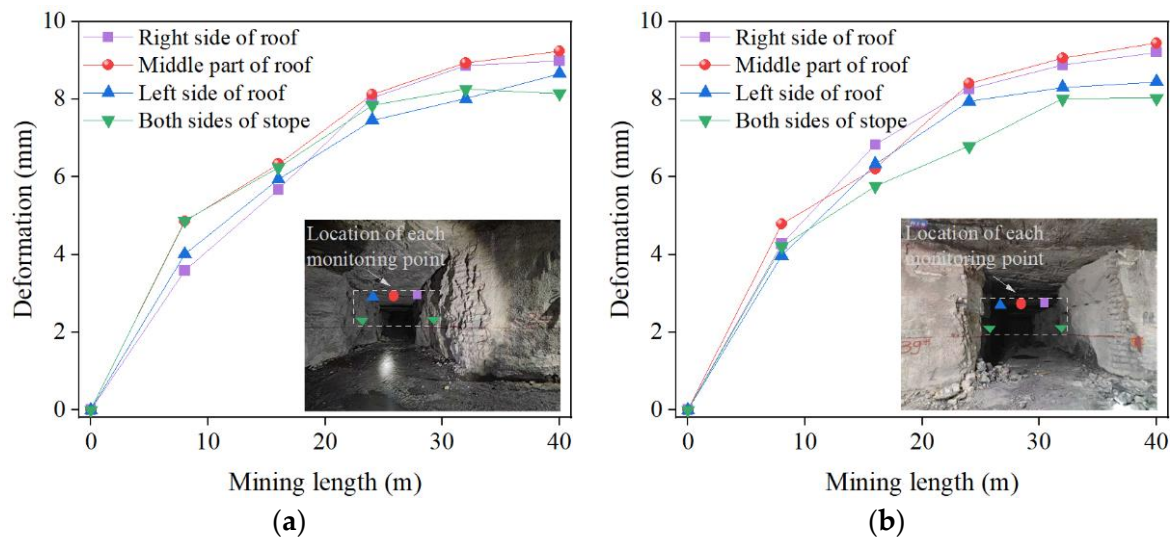
Figure 9. Comparison of calculation and measurement values: (**a**) load, (**b**) stress.

5. Conclusions

Through field measurements and theoretical analysis, the top plate force deformation characteristics of the underhand drift cut-and-fill stopping mining method were studied and the mechanical model of the filling body was constructed, and the following conclusions were mainly obtained:

(1) With the increase in mining length, the load on the CPB roof tends to increase and then decrease and finally stabilize, while the stress–strain on the CPB roof tends to increase and then stabilize. The closer to the lower surface of the CPB roof, the higher the load and stress–strain.

(2) As the span of the stope increases, the load on the CPB roof tends to increase linearly. As the length of the stope increases, the load on the CPB roof tends to increase rapidly and then stabilize. When the length of the stope exceeds 150 m, the load on the CPB roof reaches the extreme value.

(3) The overlying load variation law of the CPB roof obtained based on the Classical Janssen pressure theory agrees with the field measurement, and the error with the measured value is less than 6%. The calculation results of the mechanical model of the filling body constructed by the thick plate theory have an error of no more than 5% with the field measurements.

(4) Applying the research results to Jinchuan Group's third mine, the span of the stope can be expanded from 5 m to 6 m under the strength standard of the existing filling body, which results in 20% higher output, 11.4% lower mining cost and 16.3% higher mining efficiency. The research results are of great significance to the sustainable development of the mine.

Author Contributions: Writing—original draft preparation, Y.H.; writing—review and editing, B.H.; visualization, B.Z.; supervision, K.L. All authors have read and agreed to the published version of the manuscript.

Institutional Review Board Statement: Not applicable.

Informed Consent Statement: Not applicable.

Data Availability Statement: The data generated in this study are available upon request.

Conflicts of Interest: The authors declare no conflict of interest.

References

1. Li, Y.; Zhang, Y.; Yang, L.; Du, F.; Sai, L.; Zhang, B. Decoupling analysis of China's mining industrial development and water usage: Based on production-based and consumption-based perspectives. *J. Clean. Prod.* **2022**, *385*, 135668. [CrossRef]
2. Hosseinpour, M.; Osanloo, M.; Azimi, Y. Evaluation of positive and negative impacts of mining on sustainable development by a semi-quantitative method. *J. Clean. Prod.* **2022**, *366*, 132955. [CrossRef]
3. Nguyen, H.; Vo, D.; Bui, H.; Le, T.; Vo, B. An efficient approach for mining weighted uncertain interesting patterns. *Inform. Sci.* **2022**, *615*, 1–23. [CrossRef]
4. Wang, L.; Lu, Z.; Chen, D.; Liu, Q.; Chu, P.; Shu, L.; Ullah, B.; Wen, Z. Safe strategy for coal and gas outburst prevention in deep-and-thick coal seams using a soft rock protective layer mining. *Saf. Sci.* **2020**, *129*, 104800. [CrossRef]
5. Dong, L.; Sun, D.; Shu, W.; Li, X. Exploration: Safe and clean mining on Earth and asteroids. *J. Clean. Prod.* **2020**, *257*, 120899. [CrossRef]
6. Jian-Ming, Z.; Zhong-Wen, M.; Jin-Hai, X.; Ji-Nan, W. Research on the Technology of Filling and Repeated Mining in Thick Coal Seam Affected by Small Mine Gob Area. *Procedia Eng.* **2011**, *26*, 1150–1156. [CrossRef]
7. Shiqing, N.; Qian, G.; Zenghui, L. Numerical Simulation of Fluid-Solid Coupling in Surrounding Rock and Parameter Optimization for Filling Mining. *Procedia Eng.* **2011**, *26*, 1639–1647. [CrossRef]
8. Sirait, B.; Wattimena, R.K.; Widodo, N.P. Rockburst Prediction of a Cut and Fill Mine by using Energy Balance and Induced Stress. *Procedia Earth Planet. Sci.* **2013**, *6*, 426–434. [CrossRef]
9. Ran, J.J. Safe mining practices under wide spans in underground non-caving mines—Case studies. *Int. J. Min. Sci. Technol.* **2019**, *29*, 535–540. [CrossRef]
10. Pagé, P.; Li, L.; Yang, P.; Simon, R. Numerical investigation of the stability of a base-exposed sill mat made of cemented backfill. *Int. J. Rock Mech. Min.* **2019**, *114*, 195–207. [CrossRef]
11. Yang, Z. Key Technology Research on the Efficient Exploitation and Comprehensive Utilization of Resources in the Deep Jinchuan Nickel Deposit. *Engineering* **2017**, *3*, 559–566. [CrossRef]
12. Porter, T.M.M. Regional tectonics, geology, magma chamber processes and mineralisation of the Jinchuan nickel-copper-PGE deposit, Gansu Province, China: A review. *Geosci. Front.* **2016**, *7*, 431–451. [CrossRef]
13. Jiang, Q.; Zhong, S.; Pan, P.; Shi, Y.; Guo, H.; Kou, Y. Observe the temporal evolution of deep tunnel's 3D deformation by 3D laser scanning in the Jinchuan No. 2 Mine. *Tunn. Undergr. Sp. Tech.* **2020**, *97*, 103237. [CrossRef]
14. Yan, R.; Yin, S.; Zhang, H.; Wang, L.; Chen, D. Effect of superplasticizer on the setting behaviors and mechanical properties of tailings-waste rock cemented paste backfills. *Case Stud. Constr. Mater.* **2023**, *18*, e1714. [CrossRef]
15. Hughes, P.B.; Pakalnis, R.; Hitch, M.; Corey, G. Composite paste barricade performance at Goldcorp Inc. Red Lake Mine, Ontario, Canada. *Int. J. Min. Reclam. Environ.* **2010**, *24*, 138–150. [CrossRef]
16. Ma, S.; Hu, J.; Qin, Y.; Ren, Q.; Yang, D. Bearing mechanism and thickness optimization of ore roof in bauxite stope. *T. Nonferr. Metal. Soc.* **2022**, *32*, 285–295. [CrossRef]
17. Zhao, X.; Zeng, N.; Deng, L.; Zhu, Q.; Zhao, Y.; Yang, S. Optimization Drift Support Design Based on Engineering Geological and Geotechnical Analysis in Deep Hard-Rock Mine: A Case Study. *Appl. Sci.* **2022**, *12*, 10224. [CrossRef]
18. Zhang, H.; Xue, Y.; Li, Y.; Yin, J. Study on Initial Fracture Characteristics of the Main Roof in Fully Mechanized Caving Mining of Inclined Coalbed. *Sustain. -Basel* **2022**, *14*, 13782. [CrossRef]
19. Talibe Keita, A.M.; Jahanbakhshzadeh, A.; Li, L. Numerical analysis of the stability of arched sill mats made of cemented backfill. *Int. J. Rock Mech. Min.* **2021**, *140*, 104667. [CrossRef]
20. Mitchell, R.J. Sill mat evaluation using centrifuge models. *Min. Sci. Technol.* **1991**, *13*, 301–313. [CrossRef]
21. Sobhi, M.A.; Li, L.; Aubertin, M. Numerical investigation of earth pressure coefficient along central line of backfilled stopes. *Can. Geotech. J.* **2017**, *54*, 138–145. [CrossRef]
22. Jahanbakhshzadeh, A.; Aubertin, M.; Li, L. A New Analytical Solution for the Stress State in Inclined Backfilled Mine Stopes. *Geotech. Geol. Eng.* **2017**, *35*, 1151–1167. [CrossRef]
23. Falaknaz, N.; Aubertin, M.; Li, L. Numerical analyses of the stress state in two neighboring stopes excavated and backfilled in sequence. *Int. J. Geomech.* **2015**, *15*, 04015005. [CrossRef]
24. Deng, H.; Liu, Y.; Zhang, W.; Yu, S.; Tian, G. Study on the Strength Evolution Characteristics of Cemented Tailings Backfill from the Perspective of Porosity. *Minerals* **2021**, *11*, 82. [CrossRef]
25. Lv, W.; Wu, Y.; Ming, L.; Yin, J. Migration Law of the Roof of a Composited Backfilling Longwall Face in a Steeply Dipping Coal Seam. *Minerals* **2019**, *9*, 188. [CrossRef]
26. Chang, Q.; Sun, Y.; Leng, Q.; Liu, Z.; Zhou, H.; Sun, Y. Stability Analysis of Paste Filling Roof by Cut and Fill Mining. *Sustain. -Basel* **2021**, *13*, 10899. [CrossRef]
27. Sun, J. Mechanics criterion and factors affecting overburden stability in solid dense filling mining. *Int. J. Min. Sci. Technol.* **2017**, *27*, 407–413. [CrossRef]
28. Zhu, H.; Han, L.; Meng, Q.; Tian, M.; Meng, L.; Zhao, Z. Determining the minimum thickness of a crown pillar and optimizing the cross-sectional size of point pillars for the safe exploitation of a subsea gold mine. *Arab. J. Geosci.* **2021**, *14*, 1275. [CrossRef]

29. Xu, S.; Liang, R.; Suorineni, F.T.; Li, Y. Evaluation of the use of sublevel open stoping in the mining of moderately dipping medium-thick orebodies. *Int. J. Min. Sci. Technol.* **2021**, *31*, 333–346. [CrossRef]

30. Chang, Q.; Tang, W.; Xu, Y.; Zhou, H. Research on the width of filling body in gob-side entry retaining with high-water materials. *Int. J. Min. Sci. Technol.* **2018**, *28*, 519–524. [CrossRef]

31. Shi, X.; Gou, Y.; Chen, X.; Luo, J. Determination and application of the backfill thickness in the residual ore recovery of crown and sill pillar. *Caikuang Yu Anquan Gongcheng Xuebao/J. Min. Saf. Eng.* **2016**, *33*, 1080–1088.

32. Wu, A.; Zhang, A.; Wang, H.; Li, G.; Rong, K. The mechanical model for the paste false roof and finite element analysis. *Caikuang Yu Anquan Gongcheng Xuebao/J. Min. Saf. Eng.* **2017**, *34*, 587–593.

33. Sun, Q.; Zhang, J.; Zhou, N. Study and discussion of short- strip coal pillar recovery with cemented paste backfill. *Int. J. Rock Mech. Min.* **2018**, *104*, 147–155. [CrossRef]

34. Raffaldi, M.J.; Seymour, J.B.; Richardson, J.; Zahl, E.; Board, M. Cemented Paste Backfill Geomechanics at a Narrow-Vein Underhand Cut-and-Fill Mine. *Rock Mech. Rock Eng.* **2019**, *52*, 4925–4940. [CrossRef]

35. Basarir, H.; Sun, Y.; Li, G. Gateway stability analysis by global-local modeling approach. *Int. J. Rock Mech. Min.* **2019**, *113*, 31–40. [CrossRef]

36. Sun, Y.; Li, G.; Basarir, H.; Karrech, A.; Azadi, M.R. Laboratory evaluation of shear strength properties for cement-based grouted coal mass. *Arab. J. Geosci.* **2019**, *12*, 690. [CrossRef]

37. Sun, Y.; Li, G.; Zhang, J.; Qian, D. Stability Control for the Rheological Roadway by a Novel High-Efficiency Jet Grouting Technique in Deep Underground Coal Mines. *Sustain. -Basel* **2019**, *11*, 6494. [CrossRef]

38. Chang, Q.; Sun, X.; Dong, X.; Shao, S. Stability analysis of cemented paste backfill false roof in highwall mining: A case study. *Desalin. Water Treat.* **2021**, *219*, 96–102. [CrossRef]

39. Sun, Y.; Li, G.; Zhang, N.; Chang, Q.; Xu, J.; Zhang, J. Development of ensemble learning models to evaluate the strength of coal-grout materials. *Int. J. Min. Sci. Technol.* **2021**, *31*, 153–162. [CrossRef]

40. Ma, F.; Liu, F.; Guo, J.; Lu, R.; Guo, H.; Kou, Y. Backfill stability analysis of steep dip mine using filling method. *J. Eng. Geol.* **2018**, *26*, 1351–1359.

41. Sears, M.M.; Slaker, B.; Rashed, G.; Winfield, J. Numerical model validation and analysis of a dipping limestone pillar using FLAC3D. In *53rd U.S. Rock Mechanics/Geomechanics Symposium, Brooklyn, NY, United States, 2019*; American Rock Mechanics Association (ARMA): Brooklyn, NY, USA, 2019.

42. Sun, Y.; Bi, R.; Chang, Q.; Taherdangkoo, R.; Zhang, J.; Sun, J.; Huang, J.; Li, G. Stability Analysis of Roadway Groups under Multi-Mining Disturbances. *Appl. Sci.* **2021**, *11*, 7953. [CrossRef]

43. Wu, K.; Shao, Z.; Qin, S.; Wei, W.; Chu, Z. A critical review on the performance of yielding supports in squeezing tunnels. *Tunn. Undergr. Sp. Tech.* **2021**, *115*, 103815. [CrossRef]

44. Wu, K.; Shao, Z.; Sharifzadeh, M.; Hong, S.; Qin, S. Analytical computation of support characteristic curve for circumferential yielding lining in tunnel design. *J. Rock Mech. Geotech. Eng.* **2022**, *14*, 144–152. [CrossRef]

45. He, M.; Wang, Q. Excavation compensation method and key technology for surrounding rock control. *Eng. Geol.* **2022**, *307*, 106784. [CrossRef]

46. Shahinpoor, M. Exact bounds on average granular pressures in a general bin model. *Appl. Math. Model.* **1981**, *5*, 185–188. [CrossRef]

47. Peng, M.; Peng, H. The ultimate bearing capacity of shallow strip footings using slip-line method. *Soils Found.* **2019**, *59*, 601–616. [CrossRef]

48. Yang, L.; Hou, C.; Zhu, W.; Liu, X.; Yan, B.; Li, L. Monitoring the failure process of cemented paste backfill at different curing times by using a digital image correlation technique. *Constr. Build. Mater.* **2022**, *346*, 128487. [CrossRef]

49. Namdar, A. The crack zone simulation of clay backfill under seismic load. *Procedia Struct. Integr.* **2022**, *39*, 57–64. [CrossRef]

50. Xu, W.; Tian, M.; Li, Q. Time-dependent rheological properties and mechanical performance of fresh cemented tailings backfill containing flocculants. *Miner. Eng.* **2020**, *145*, 106064. [CrossRef]

51. Yin, S.; Hou, Y.; Chen, X.; Zhang, M. Mechanical, flowing and microstructural properties of cemented sulfur tailings backfill: Effects of fiber lengths and dosage. *Constr. Build. Mater.* **2021**, *309*, 125058. [CrossRef]

52. Bertocchi, E.; Mantovani, S.; Ciavarella, M. A simple method of analysis of partial slip in shrink-fitted shafts under torsion. *Int. J. Mech. Sci.* **2018**, *142–143*, 541–546. [CrossRef]

53. Höller, R.; Aminbaghai, M.; Eberhardsteiner, L.; Eberhardsteiner, J.; Blab, R.; Pichler, B.; Hellmich, C. Rigorous amendment of Vlasov's theory for thin elastic plates on elastic Winkler foundations, based on the Principle of Virtual Power. *Eur. J. Mech. A/Solids* **2019**, *73*, 449–482. [CrossRef]

54. Senjanović, I.; Vladimir, N.; Tomić, M. On new first-order shear deformation plate theories. *Mech. Res. Commun.* **2016**, *73*, 31–38. [CrossRef]